MDPI

Article

Quantification of Force and Torque Applied by a High-Field Magnetic Resonance Imaging System on an Ultrasonic Motor for MRI-Guided Robot-Assisted Interventions

Peyman Shokrollahi [1,2,*], **James M. Drake** [1,2] and **Andrew A. Goldenberg** [1,3]

1   Institute of Biomaterials and Biomedical Engineering, The University of Toronto, Rosebrugh Building, 164 College Street, Room 407, Toronto, ON M5S3G9, Canada; james.drake@sickkids.ca (J.M.D.); golden@mie.utoronto.ca (A.A.G.)
2   The Hospital for Sick Children, Division of Neurosurgery, 555 University Avenue, Room 1504, Toronto, ON M5G1X8, Canada
3   Department of Mechanical and Industrial Engineering, The University of Toronto, 5 King's College Road, Toronto, ON M5S3G8, Canada
*   Correspondence: peyman.shokrollahi@mail.utoronto.ca; Tel.: +1-416-617-3034

Abstract: The risk of accidental dislodgement of robot-operated surgical mechanisms can lead to morbidity or mortality. The force and torque applied by a 3.0-tesla scanner on an ultrasonic motor are not fully known. The force and torque may displace the motor, which is not fully magnetic resonance imaging (MRI)-compatible but can be safely used in MR environments. A suspension apparatus was designed to measure the angles of deflection and rotation applied to the motor by MR magnetic fields. Three orientations and two power states of the motor were assessed inside the MR bore. The displacement force and torque were measured at eight locations with respect to the bore. The displacement force on the motor from 10 cm outside the magnet bore to 20 cm inside the bore ranged from 3 to 7 gF. The experimental measurements are in agreement with the theoretical values. Running the motor altered the force by 1 gF. The force does not significantly change when the MRI scanner is on. Considerable displacement force is applied to the motor, and no deflection torque is observed. Quantified values can be used to solve dynamic equations for robotic mechanisms intended for MRI-guided operations.

1. Introduction

Robots that are compatible with magnetic resonance imaging (MRI-compatible) will revolutionize the safety and efficiency of surgical operations by enhancing dexterity in a digitized imaging environment and providing precise positioning tools. By exploiting MRI, which is a versatile and indispensable imaging modality, these robots can enhance a surgeon's dexterity and stamina by allowing superior spatial resolution and geometric accuracy [1]. The excellent ability of MRI for localizing and robots for targeting pathologies will provide additional avenues for developing computational methods and MRI-guided interventions. Surgical instruments can be tracked in real-time while overcoming the deformation of tissues and the spatial constraints of high-resolution closed-bore MRI systems [2]. However, to perform surgery safely with high precision and full controllability, robots must have accurate actuators operating inside the MR environment [3,4].

The applied force of the MR field causes displacement force and deflection torque, resulting in unwanted actuator motion that limits the accuracy of the actuated tool and increases the safety risk for patients. Interactions may result in serious injury or death to patients. Fatality due to the displacement of tools has been previously reported [5]. The dislodgement of the robot's end effector in tissues during MR-guided interventions is extremely hazardous, particularly if the end effector is located near important vascular or neural tissues or other critical tissues. Therefore, this study focuses on characterizing the force applied by the magnetic fields of a scanner on an ultrasonic motor (USM).

The effects of MR force fields on USM performance are not completely understood. For example, the applied displacement force and deflection torque have not been fully quantified for high-field ($\geq$3 T) MRI systems. Consequently, in the context of safety, although actuators may not physically contact a patient's organs, they are connected via links that can move the end effector inside the patient's body. Therefore, unwanted dislodgement of the actuators can cause unpredictable dislodgment of other links and, consequently, of the end effector.

As we analyzed the force signals generated by the USM itself in our previous work [6]. In that study, the generated axial force of the USM was evaluated. The current study focuses on the external force that is applied by the scanner on the USM. Most previous studies have concentrated on safety issues caused by displacement force and deflection torque because safety concerns have limited the use of MRI for many patients and with various devices. As reported in Scientific Reports in 2015, approximately 300,000 patients are denied MRI each year because of these limitations [7]. Because the development of MRI-compatible tools is in a relatively early stage, the lack of knowledge regarding MRI-compatible tools and devices has resulted in the inability of patients to receive many possible benefits, including accurate diagnosis and treatment.

In addition, projectile effects account for 10% of MRI-related accidents; therefore, MRI safety regulations mandate the exclusion of many essential tools from the MR environment, including surgical robots [8]. Projectile effects are not the only reason that conventional robots are banned from MR environments; unwanted movements of robot components also limit the accuracy of surgical operations. However, the precise operation of robots depends on accurate motion of actuators and the end effector. Only three types of actuators are MRI-compatible: hydraulic, pneumatic, and ultrasonic actuators.

USMs led to unsatisfactory results when they were first used in MRI. For example, USMs interacted with the MRI scanner, inducing noise in the images and generating heat. Lack of MRI compatibility led researchers to shift their focus from USMs to pneumatic actuators in the development of surgical robots for compatibility issues. Although pneumatic and hydraulic systems address a few of the compatibility issues, they cannot provide the numerous advantages of USMs. USMs are highly advantageous because they have a high degree of precision, small size and a non-magnetic mode of operation [9].

However, unwanted motion of USMs limits their accuracy and increases the safety risk for patients [10]. The effects of MRI force fields on motor performance are not fully known. For example, the applied force and torque have not been fully quantified for high-field ($\geq$3 T) MRI systems. The risk of accidental dislodgement must be minimized because it can lead to morbidity or mortality. Although the actuators may not physically contact a patient's organs, the actuators are connected via links that can move the end effector inside the patient's body. Therefore, unwanted dislodgement of the actuators can cause unpredictable dislodgment of other links and, consequently, the end effector.

The force of attraction exerted by MRI on USMs has not been fully measured while such motors are running in their operational states, which include clockwise (CW) when the motor's shaft rotates in clockwise direction, standby when the shaft is stalled, counterclockwise (CCW) when it rotates in the CCW direction, or when the motors themselves are in motion on the operating table under MRI.

It is imperative to assess the magnetic field attraction force on a USM to ascertain the potential risks and degree of compatibility with MRI [5]. Engineering design criteria with effective safety standards can be established by quantifying the displacement force along with other effects of MRI on

the motor, such as temperature changes, and the consequences for image quality [11]. Assessment of the displacement force can also be used to formulate dynamics equations for robot mechanisms [12,13].

In addition, inclusion of the force applied by magnetic fields in dynamic equations (i.e., equations of motion) enhances computational accuracy in robot analysis, simulation, and control. The inclusion of this force is particularly important for enhancing the computational efficiency of complex robotic mechanisms operating at high speeds and for the real-time control of mechanisms and is also used in formulating algorithms for developing and implementing these mechanisms.

The displacement force should be measured to adjust the force errors caused by external forces (MRI) on the actuators. These errors can be used to adjust and control the force for tactile feedback systems. Displacement force information is also necessary to calibrate a tactile sensor [14].

This study investigates the displacement force and torque applied to an ultrasonic motor at various bore locations using the designed apparatus presented in the Materials and Methods. The experimental outcomes are presented in the Results for three orientations of the motor inside the bore and for two states (on and off). The significance of the results and findings are discussed in the Discussion, and a brief conclusion, which integrates the results and discussion, is presented in the Conclusion.

2. Materials and Methods

Two types of movement of an object induced by a magnetic field were investigated: translational movement (displacement) and rotational movement (torque). These movements both result from the force applied by the static gradient field B_0, the spatial gradient of the static magnetic field B_0, and the spatial gradient field of the gradient coil.

The amplitude of the displacement force is proportional to the magnitude of the gradient field, and the maximum gradient field is present near the portal. The magnetic torque is a result of the magnetic field strength, and the amplitude of the torque is proportional to the field strength. The maximum field strength is present at the isocenter, where the gradient is nearly zero [5].

The displacement force of the MRI fields was measured to quantify the effect of MRI on a USM. The displacement force needs to be calculated while the scanner is both off and on. This force was measured while the motor was in operation. The design of a measurement tool and the approach used to measure the force are described below.

2.1. Theoretical Evaluation

The maximum displacement force, applied force, and deflection torque can be calculated as follows [15]:

$$F_z = \frac{\chi V}{\mu_0} B_0 \frac{\partial B}{\partial z} \tag{1}$$

$$T = \frac{V B_0^2}{2\mu_0} \frac{\partial B}{\partial z} \Delta\chi \sin 2\theta \tag{2}$$

where V is the volume of the object, $\Delta\chi$ is the susceptibility difference, and θ is the angle between the magnetization vector and the magnetic flux density (B_0). The constant, μ_0, is referred to as the permeability of free space and has a value of $4\pi \times 10^{-7}$ H/m. This model is for a spherical object that is sufficiently small that the following assumptions may be made: (i) B_0 and χ are constant values, and (ii) χ is very small and has no effect on the field.

When a motor is placed in an MRI field, the spatial gradient of the static magnetic field, B_0, applies force and torque on the motor. Although B_0 is constant (3 T) around the area of the isocenter, the magnitude of the magnetic field decreases as the distance from the isocenter increases. The fringe filed is the peripheral magnetic field outside the scanner bore. The scanners also have extra windings to minimize the stray field, i.e., a magnetic field whose intensity varies with distance to minimize the magnetic-field effects in the vicinity of the scanner for safety reasons. The spatial gradient is different from gradients generated by coils. The former gradient is generated by the static gradient

of the magnet and is always present, whereas the latter is observed only during scanning. Because the MRI system must be confined to a specific area to minimize exposure of the public to the high magnetic field, the field outside the magnet is suppressed. Using this shielding technique generates a spatial gradient of the static magnetic field B_0 in which the attraction force is exponentially increased. The spatial gradient of the gradient coil is a time-varying magnetic field generated by the coils for spatial encoding of the MRI signals during scanning [16].

In the calculation of force and torque, the effects of "the spatial gradient of the gradient coil" are not fully known. These effects were experimentally analyzed in this study. However, the spatial gradient of the static magnetic field, B_0, is considerably large and should be considered in the calculations. Its applied force results in dislodgement of a robot's end effector.

According to the specification of the field distribution of the 3 T Achieva system, which is given for few points around the scanner, the field distribution can be numerically approximated to evaluate force at the later stage using (1). Figure 1 illustrates the approximated spatial (B_0) field distribution in the *z* direction, that is, the bore axis. The B_0 field distribution is used in (1) to calculate force. In Figure 1, the field distribution specified by the 3 T Achieva system is indicated by stars, and the fitted curve is indicated by the solid line. The values of the field distribution inside the bore have not been provided by the manufacturer. Therefore, it was assumed that the magnetic field inside the bore is constant (approximately of 3 T). The variation of this value inside the bore has an insignificant impact on the force calculation independent of the manufacturing specifications. Interpolation via "piecewise cubic Hermite interpolating polynomial" was selected from the curve fitting toolbox of MATLAB 2013b to fit a curve to the given values in the *z* direction. The fitted curve models the change in the field with an R-squared value of approximately 1. The approximated cubic polynomials derived through this model were used to calculate the force using (1). In this calculation, it was assumed that the field of approximately 3 T is homogeneous and steady inside the bore up to 75 cm from the center of the bore [17]. The force at the isocenter is theoretically zero. The calculation was performed for the following four parts of the motor with considerable susceptibility: shaft, rear case, front case, and stator ring. Other parts of the motor were not included in these calculations because of their insignificant susceptibility. Table 1 shows the material properties used for the theoretical evaluation.
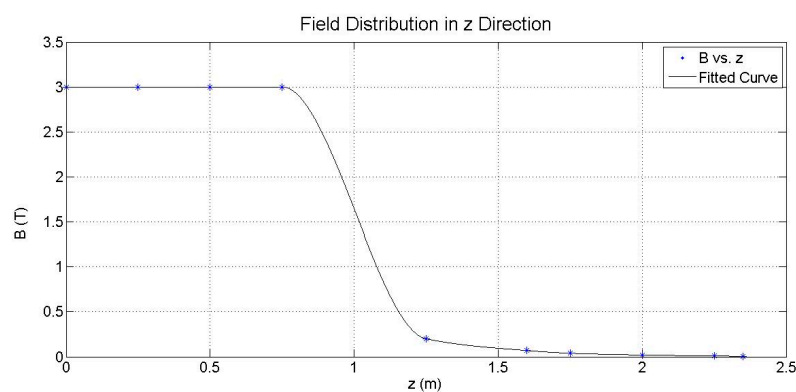

Figure 1. Approximated spatial (B_0) field distribution in the *z* direction.

Table 1. Material Properties Used In the Theoretical Evaluation of Displacement Force.

	Material	Ø	Volume
Brass Shaft	Brass	2.2×10^{-4} [a]	5.3×10^{-7}
Front Case	Aluminum	2.2×10^{-5} [b]	1.2×10^{-6}
Rear Case	Aluminum	2.2×10^{-5}	8.1×10^{-6}
Stator Ring	Brass	2.2×10^{-4}	1.2×10^{-4}

[a] [18]; [b] [19].

The suggested formula is estimated for small objects that do not affect the external magnetic field. In theory, the effects of the induced magnetization of small objects on the external magnetic field can be ignored. In addition, the magnetic field is assumed to be theoretically infinite to obtain (1) and (2). However, the dimensions of the motor are not insignificant compared to the scanner's magnet, and the motor perturbs the field. Therefore, the demagnetizing factor (known as the shape factor) should be considered in (1) to approximate the proper theoretical value of force. The motor shape was approximated by a sphere. Typically, the force is proportional to the inverse of the demagnetizing factor. A demagnetizing factor of 1/3, reported for spheres, was used in this calculation because it has the largest impact on calculating force compared to other demagnetizing factors [20]. Table 2 shows the total force applied to the motor.

Table 2. Theoretical Evaluation of Displacement Force.

Motor Distance from Portal (cm)	Outside Bore			Portal	Inside Bore			Isocenter
	+110	+20	+10	0	−10	−20	−40	100
Displacement Force (gF)	0	5.35	7.76	8.80	7.41	3.13	0	0

The torque is theoretically evaluated using (2). The induced magnetization vector in the materials (**M**) and **B** are in the same direction, and the angle θ is zero because the motor materials are assumed to be isotropic, i.e., the induced **M** is parallel to the direction of the external field. Therefore, the deflection torque is zero.

2.2. Suspension Apparatus

To measure the displacement force, a suspension apparatus was designed and implemented to support the motor in the MRI bore (Figure 2). The apparatus was composed of an arch, a base frame, a plate, threads, a piece of graph paper, and a marker. The arch was installed on the base frame to stabilize the system. The plate was suspended from the center of the arch by three suture threads. To fix the position of the motor in the plate, the motor was placed in the plate filled with dough (Play-Doh). The marker was glued below the plate to indicate the deflection angle on the graph paper taped on the frame base.
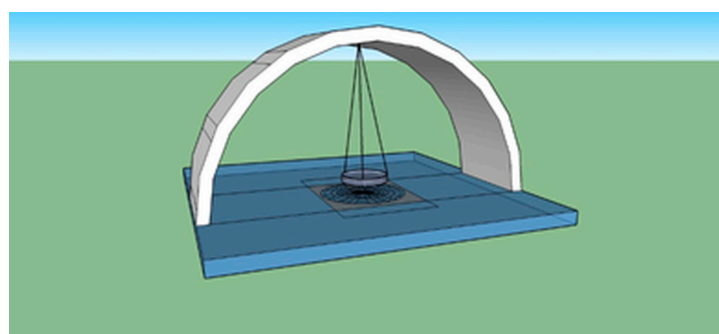

Figure 2. Schematic of the suspended apparatus used to measure the displacement force and torque.

The following MRI-compatible materials were used: a stainless-steel arch, a polyethylene terephthalate (PET) plate, silk suture threads, polar graph paper, a glass frame base, and a wooden marker. The dimensions were as follows. The plate was 6.5 cm in diameter with a depth of 1.5 cm, the threads were each 25 cm in length, and the height of the marker was 1 cm. The total height from the suspension node to the tip of marker was 27 cm. The plate and colored dough weighed 30 g. The motor system, including the motor itself, encoder, and part of the shielding, weighed 195 g. The plate, threads and marker weighed 5 g.

Polar graph paper was used to evaluate the deflection angle instead of the previously proposed wooden protractor [21]. The polar graph was in concentric form at a distance of 3 mm and a radial distance of 5°. The distance between two concentric circles was divided into four segments. To reduce the complexity of the reading, the number of concentric circles was reduced to 22 with 12 primary spokes and 72 secondary spokes labeled in degrees.

This apparatus is advantageous compared with the proposed methods in [11,21]. The bulky motor (compared with the small volumes of implants or projectiles) can be placed on the spacious plate. The suspended plate can tolerate more weight than a suspension with only a single suture. The polar graph has a higher visual reading accuracy than a protractor. The reading error of the polar system is ±0.25°, whereas that of a protractor is ±0.5°. This measuring accuracy was obtained according to quarter divisions between the lines and circles on graph paper.

2.3. Approach

A USM, i.e., PUMR 40E (Piezoelectric Technology Co., Ltd., Seoul, Korea), was placed on the plate. The deflection angles were measured using a 3T Achieva scanner (Philips Healthcare, Best, The Netherlands). The deflection angle was evaluated by manual reading of the marker on the polar graph located at the bottom of apparatus (Figure 2). An indicator was attached to the marker to indicate the rotation of the marker for torque measurements. The torque was measured about the axis perpendicular to the plane of the graph paper (Figure 2). Rotations about the other two axes were measured as the deviations of the markers on the circles of the polar graph. The device was placed on the scanner tabletop on foam rubber (Philips Healthcare, Best, The Netherlands) to locate the motor at the level of the bore's centerline because the field is purely axial with no tangential components along this line [22]. The horizontal alignment of the frame base was also verified using a spirit level before beginning the experiment.

The deflection angle and rotation angle were measured along the bore's centerline at eight locations (Table 3 and Figure 2). For each location, the experiment was performed at least three times by two observers [11,17]. Before each measurement, the apparatus was calibrated at an origin point 110 cm from the portal outside the bore, where no displacement was observed, and was carefully moved to the location of interest.

Table 3. Locations of the Ultrasonic Motor with Respect to the Portal.

Location	Description
−100 cm	At the isocenter
−40 cm	Inside the bore and 40 cm from the portal
−20 cm	Inside the bore and 20 cm from the portal
−10 cm	Inside the bore and 10 cm from the portal
0	At the portal
+10 cm	Outside the bore and 10 cm from the portal
+20 cm	Outside the bore and 20 cm from the portal
+110 cm	Outside the bore and 110 cm from the portal

Additionally, the displacement force was measured on the cover surface of the scanner at the portal above the operating table, where the maximum spatial gradient of the static magnetic field B_0 was located in the 3 T Achieva system [17]. The spatial gradient of the static magnetic field B0 specifies how steeply B_0 changes as a function of position. This quantity indicates the applied attraction force on metallic objects.

The motor was oriented in three directions: the *x*-axis was parallel to the patient table and perpendicular to the bore axis, the *y*-axis of the motor's shaft was perpendicular to the patient table, and the *z*-axis was parallel to the bore axis (Figure 3).
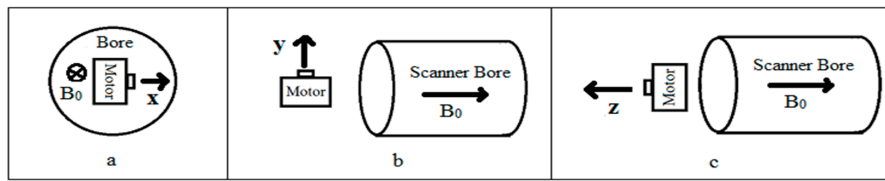
Figure 3. Motor orientations: (**a**) *x*; (**b**) *y*; and (**c**) *z*.

2.4. Displacement Force Measurement

The displacement force was evaluated using (3), where m is the total mass of the motor system and the suspended part of the suspension apparatus (i.e., plate, marker, and dough). g is 9.8 m/s^2, and θ is the deflection angle from the vertical axis. The sum of the suspended masses was considered in the force calculation. The error was measured by considering the total mass.

$$F = mg \tan \theta \tag{3}$$

2.5. Deflection Torque Measurement

The torque was measured using the same method as in [23] except that the system was placed at the center of the bore. The angle of rotation, φ, was measured, and the torque was then calculated using (4). The angle of rotation was measured by evaluating the marker's rotation along its axis on the suspension plate.

$$\tau = mLg \sin \varphi \tag{4}$$

3. Results

3.1. Displacement Force Measurement

3.1.1. Displacement Force in a Static Magnetic Field

The displacement force was measured at various locations with respect to the scanner while the scanner was off. Figure 4 presents the mean values of five force measurements for three configurations (*x*, *y*, and *z*). The force was measured in gF at the locations illustrated in Figure 5. For each measurement, the apparatus was located at the distance from the bore shown in Table 3. The distance of the marker from the center of the polar graph was measured, and tan θ was calculated by dividing this distance by the height of the suspended motor from the pivot point. The maximum standard deviation was calculated as 0.3, 0.1, and 0.2 for the *x*-, *y*-, and *z*-orientations, respectively. Table 4 presents the results for the powered motor rotating clockwise (CW) and counter-clockwise (CCW) for the three configurations. The scanner was off during these measurements.

Table 4. Displacement Force (gF) of the Static Magnetic Field When the Motor Was Rotating CW and CCW in the *x*-, *y*-, and *z*-orientations.

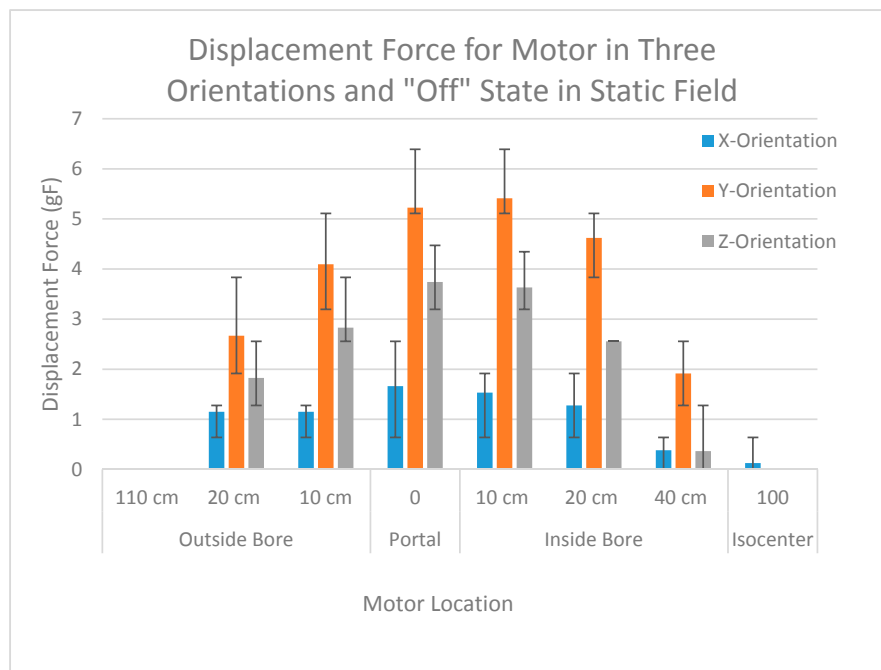| Motor Orientation	Motor Location (cm)		Outside Bore			Portal		Inside Bore			Isocenter
	Motor State		110	20	10	0	10	20	40	100
x-orientation		"Off"	0	0	0.6	1.3	1.3	1.3	0.6	0
	"On"	CW	0	0	0.6	1.3	1	1	0.6	−0.3
		CCW	0	0	0.6	1.3	1.5	1.5	0.7	+0.3
y-orientation		"Off"	0	3.8	5.1	6.4	6.4	5.1	2.5	0
	"On"	CW	0	3.8	5.1	5.1	5.1	3.8	1.3	−1.3
		CCW	0	4.1	5.3	7.7	7.7	6.4	3.8	+1.3
z-orientation		"Off"	0	1.2	2.5	3.8	3.8	2.6	0	0
	"On"	CW	0	1.2	2.5	3.6	3.2	2.3	−0.3	−0.3
		CCW	0	1.2	2.5	4.1	4.5	2.8	0.3	0.3

Figure 4. Displacement force on the powered-off motor in the *x*-, *y*-, and *z*-orientation in the static magnetic field.
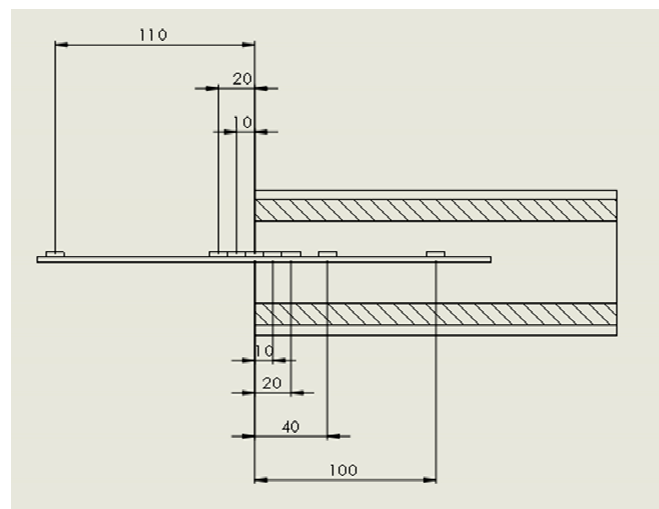

Figure 5. Locations of motor from the MRI portal.

3.1.2. Displacement Force While the Motor is in Motion inside a Static Magnetic Field

The displacement force was approximately 12.8 gF when the motor was in motion. The motor was placed in the suspension system and was moved by moving the operating table at the maximum speed (approximately 16 cm/s) in and out of the bore. The maximum displacement force was applied to the motor when it was moved between 10 cm outside the bore and 20 cm inside the bore.

3.1.3. Displacement Force during Scanning

The values of the displacement force in various configurations and states are compared in Figure 6. "Scanner on" in this figure refers to the MRI state in which the three sequences were applied. The results obtained for the three different sequences were similar. Thus, these results are shown in the figure as

"scanner on". The motor was located in the *y*-orientation and was tested in the "off" and "on" states and in both the CW and CCW directions.

3.1.4. Displacement Force about the Maximum Gradient Field on the Cover Surface

Figure 7 shows the range of displacement forces measured at the surface of the magnet's front cover where the gradient field is maximum. The apparatus was situated such that the motor was at heights of 50 cm and 60 cm from the patient table. The motor was tested only in the "off" state and the *y*-orientation.
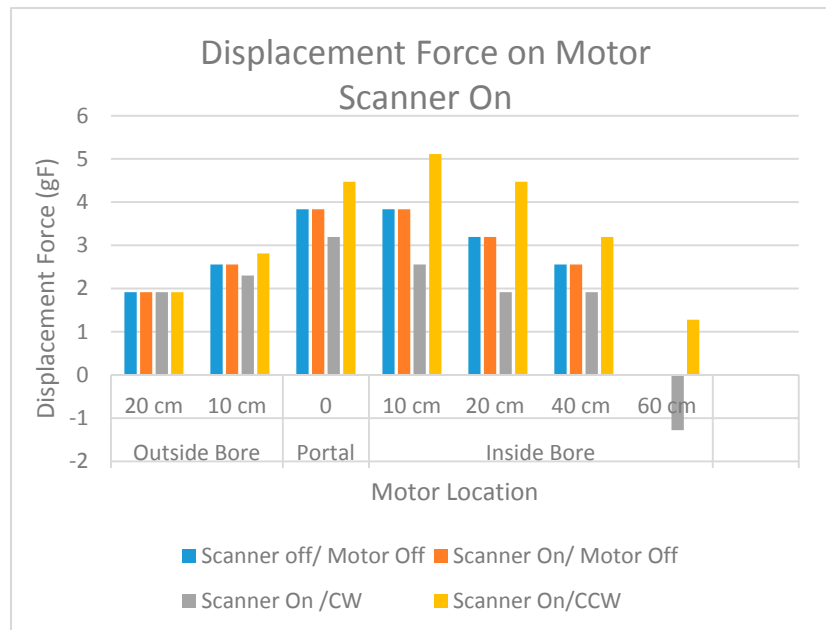

Figure 6. Displacement force on the powered-off motor in the *y*-orientation while the scanner was on and off.
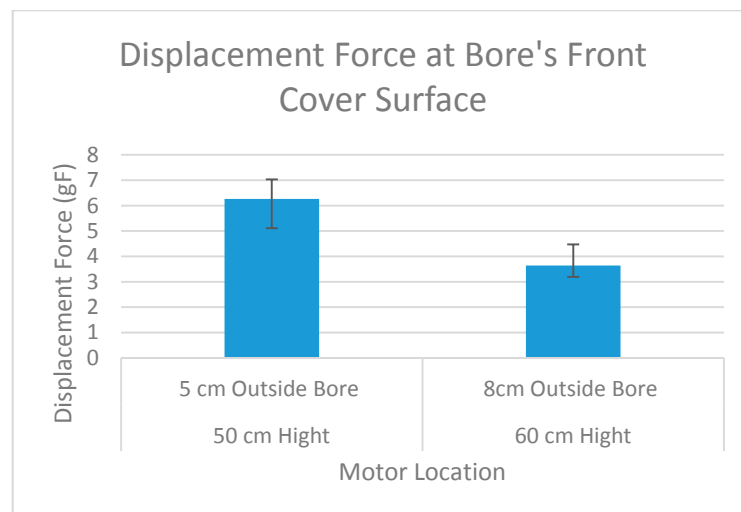

Figure 7. Displacement force on the motor in the *y*-orientation at the surface of the front cover of the bore.

3.1.5. Deflection Torque Measurement

The angle of rotation and subsequent torque measurements were insignificant in all cases, i.e., in all motor states and configurations and in all scanning states (on and off).

4. Discussion

The evaluated theoretical values, as shown in Table 2, are within the same range as that of the experimental values. Table 2 shows the theoretically evaluated forces, which were the target values for various locations inside the bore. The deviation between the evaluated theoretical and experimental values is due to several reasons. First, the magnetization factor was selected for a spherical shape as the maximum value of the shape factor. Second, the motor's stator ring was approximated and its exact volume and material are not known. Third, the susceptibility of the materials was approximated for motor parts, which may be different in reality. Furthermore, the magnetic susceptibility of brass was estimated, as this value is not easily attainable and depends on the portions of its composites. Finally, owing to magnetization of the motor parts, internal forces exist among these parts, which were not considered in the theoretical calculations.

A static field applies an attractive force on metallic objects. The magnitude of this force is proportional to the magnitude of the magnetic field. The applied force on a motor depends on the structural composition and geometric shape of the motor's metal components, such as the aluminum case, the brass shaft, and the internal metal components of the stator (conductor ring) and encoder. However, given the inaccessibility of most of these components and thus the difficulty associated with studying them, the interactions of the MRI and actuator were studied as a system, and the force was considered the total force applied to the motor's center of mass.

The maximum displacement force when the motor was not in motion was located between 10 cm outside the bore and 20 cm inside the bore. The displacement force was highest in this region because this is where the maximum gradient was present [24]. The maximum force was not located at the portal, as had been theoretically expected. Our findings are supported by those of Kagestu, who also reported [25] the possibility of the maximum gradient not occurring at the portal. Additionally, we found that the maximum displacement force was applied at the surface of the bore's front cover (5 cm outside the bore at a height of 50 cm from the operating table) for the 3 T Achieva (Philips). However, the location of the maximum gradient and, consequently, the maximum displacement force might vary with the type of scanner.

The displacement force increased when the entire motor structure was moved. Increasing the speed of motion increased the displacement force applied to the motor by the MRI device. In this experiment, the maximum speed for moving the motor was limited to the maximum speed of the operating table. If the motor is used on a joint and moved with another actuator on a robot, motion speeds greater than the tested value would be possible and should be evaluated.

Although a deflection angle above 45° has been deemed a considerable force [26] for testing ballistic objects and metal implants, such an angle would be too high for a motor because its mass is much greater than that of these objects. The mass of tested objects is on the order of hundreds of milligrams (e.g., a Drake aneurysm clip is 630 mg). Thus, when these objects are exposed to a high magnetic field, the deflection angle is high. However, the weight of the motor in this study was approximately 195 g, which is 100 times larger than the weights of these objects. Therefore, a small deflection angle (<1°) is considered a large force on the motor.

A cutoff force for the safety of motors placed in the MRI bore has not been reported. Nevertheless, the reported force of implants in [27] provides a good reference. This study found that forces above 1 gF can be considered as high in terms of safety because the end effector of the actuated robot may come in contact with critical tissues during surgery. Implants generate a relatively small displacement force (e.g., 0.75 gF by a Drake aneurysm clip [24]). Comparing the displacement forces reported in [27] to the force applied to the motor, we conclude that the maximum displacement force (7 gF) on the motor is much larger than that reported for most implants. This force was theoretically calculated to

be reduced to 2.1 gF or 0.7 gF when the volume of the brass and aluminum case was decreased by 1/4 or when the case was replaced with silicon carbide, respectively.

The agreement between the theoretical calculation and the experimental evaluation shows that the isotropic material assumption is valid. Although a small torque may exist, its value is insignificant. The possibility of having a significant torque was evaluated by randomly rotating the motor's body inside the scanner. However, the symmetrical shape of the motor's metal components results in a balanced force on the body of the motor, which is a potential reason for the insignificant torque.

Running the motor alters the force by 1 gF. Running the motor in the CW and CCW directions causes attractive and repulsive forces on the motor of identical magnitudes in both directions. In some cases, the CW and CCW rotation directions showed different experimental results (Table 4). This difference occurred because the static magnetic field applied different forces to the shaft of the rotating motor. The orientation of the shaft is not aligned with the direction of the static field when the motor is in the x- or y-orientation. In addition, the shape of the shaft is not completely symmetrical; i.e., there is a cut part on the cylindrical structure of the shaft. Consequently, different results may be observed even when the shaft is aligned with the z-orientation.

The type of pulse sequence did not affect the displacement force. Turning the scanner on had an insignificant effect on the displacement force on the motor. There was no significant difference between the three image sequences, indicating that the spatial gradient of the gradient coil has insignificant effects on the force values. Additionally, the orientation of the scan did not affect the displacement force.

The minimum effective external force varies depending on the speed, weight, and arm length of the robot. In addition, the actuators are typically attached to the links, which are in motion or are not stabilized themselves. Therefore, the applied force on the links should be considered when solving dynamic equations for the robot.

We have studied other aspects of MR safety and MR compatibility of these motors. Quantitative analyses of temperature change, geometric distortions of MR images, and signal-noise-ratio of USM have been reported in [28–30].

5. Conclusions

The applied displacement force on a USM actuator, as quantified here, can be used for developing robotic mechanisms during MRI. Considering the safety of patients, the induced force is significant compared with that on metal implants of an identical weight. This force can be reduced by decreasing the volume of the case conductors by 1/4 or by replacing the case conductors with silicon carbide. The applied torque induced by MRI on the motor is insignificant and can therefore be neglected. Operating the motor (motor in the "on" state) does not affect the displacement force or deflection torque.

Author Contributions: Peyman Shokrollahi conceived and designed the experiments; Peyman Shokrollahi performed the experiments; Peyman Shokrollahi analyzed the data; James M. Drake and Andrew A. Goldenberg contributed reagents/materials/analysis tools; James M. Drake and Andrew A. Goldenberg had contributions in data analysis and data interpretation. Peyman Shokrollahi wrote the paper.

Conflicts of Interest: The authors declare no conflict of interest.

References

1. Louw, D.F.; Fielding, T.; McBeth, P.B.; Gregoris, D.; Newhook, P.; Sutherland, G.R. Surgical robotics: A review and neurosurgical prototype development. *Neurosurgery* **2004**, *54*, 525–537. [CrossRef] [PubMed]
2. Elhawary, H.; Tse, Z.T.; Hamed, A.; Rea, M.; Davies, B.L.; Lamperth, M.U. The case for MR-compatible robotics: A review of the state of the art. *Int. J. Med. Robot.* **2008**, *4*, 105–113. [CrossRef] [PubMed]

3.　Masamune, K.; Kobayashi, E.; Masutani, Y.; Suzuki, M.; Dohi, K.; Iseki, H.; Takakura, K. Development of an MRI-compatible needle insertion manipulator for stereotactic neurosurgery. *J. Image Guid. Surg.* **1995**, *1*, 242–248. [CrossRef]

4.　Chinzei, K.; Hata, N.; Jolesz, F.; Kikinis, R. MR compatible surgical assist robot: System integration and preliminary feasibility study. In *Medical Image Computing and Computer-Assisted Intervention—MICCAI 2000*; Delp, S.L., DiGoia, A.M., Jaramaz, B., Eds.; Springer: Berlin, Germany, 2000; pp. 921–930.

5.　Dempsey, M.F.; Condon, B.; Hadley, D.M. MRI safety review. *Semin. Ultrasound CT MR* **2002**, *23*, 392–401. [CrossRef]

6.　Shokrollahi, P.; Drake, J.M.; Goldenberg, A.A. Comparing the effects of three MRI RF sequences on ultrasonic motors. In *World Congress on Medical Physics and Biomedical Engineering*; Jaffray, D.A., Ed.; Springer: Toronto, ON, Canada, 2015; pp. 846–849.

7.　Serano, P.; Angelone, L.M.; Katnani, H.; Eskandar, E.; Bonmassar, G. A novel brain stimulation technology provides compatibility with MRI. *Sci. Rep.* **2015**, *5*, 9805. [CrossRef] [PubMed]

8.　Joint Commission. Preventing accidents and injuries in the MRI suite. *J. Radiol. Nurs.* **2008**, *27*, 74–77.

9.　Cole, G.A.; Harrington, K.; Su, H.; Camilo, A.; Pilitsis, G.J.; Fischer, G.S. Closed-loop actuated surgical system utilizing real-time in-situ MRI guidance. In *Experimental Robotics*; Khatib, O., Kumar, V., Sukhatme, G., Eds.; Springer: Berlin, Germany, 2014; pp. 785–798.

10.　Shellock, F.G.; Crues, J.V.; Karacozoff, A.M. *MRI Issues for Implants and Devices*; Biomedical Research Publishing Group: Los Angeles, CA, USA, 2014.

11.　Eggert, S.; Kubik-Huch, R.A.; Klarhöfer, M.; Peters, A.; Bolliger, S.A.; Thali, M.J.; Anderson, S.; Froehlich, J.M. Fairly direct hit! Advances in imaging of shotgun projectiles in MRI. *Eur. Radiol.* **2015**, *25*, 2745–2753. [CrossRef] [PubMed]

12.　Featherstone, R.; Orin, D. Robot dynamics: Equations and algorithms. In Proceedings of the IEEE International Conference on Robotics and Automation, San Francisco, CA, USA, 24–28 April 2000; pp. 826–834.

13.　Luh, J.Y.S.; Walker, M.W.; Paul, R.P.C. On-line computational scheme for mechanical manipulators. *J. Dyn. Sys. Meas. Control.* **1980**, *102*, 69–76. [CrossRef]

14.　Mardasi, A.G.; Ghanbari, M.; Tehrani, M.S. Design and finite element modeling of a novel optical microsystems-based tactile sensor for minimal invasive robotic surgery. In Proceedings of the SPIE 9288, Photonics North 2014, Montreal, QC, Canada, 25 September 2014.

15.　Schenck, J.F. Physical interactions of static magnetic fields with living tissues. *Prog. Biophys. Mol. Biol.* **2005**, *87*, 185–204. [CrossRef] [PubMed]

16.　Shellock, F.G.; Kanal, E.; Gilk, T.B. Regarding the value reported for the term 'spatial gradient magnetic field' and how this information is applied to labeling of medical implants and devices. *AJR Am. J. Roentgenol.* **2011**, *196*, 142–145. [CrossRef] [PubMed]

17.　Philips. *Philips Medical Systems Technical Description: Achieva Release 3.2 Series*; Philips Medical Systems: Best, The Netherlands, 2005; pp. 3–4.

18.　Sunderland, A.; Ju, L.; McRae, W.; Blair, D.G. Reducing the magnetic susceptibility of parts in a magnetic gradiometer. *arXiv* **2007**, arXiv:0709.1323.

19.　Schenck, J.F. The role of magnetic susceptibility in magnetic resonance imaging: MRI magnetic compatibility of the first and second kinds. *Med. Phys.* **1996**, *23*, 815–850. [CrossRef] [PubMed]

20.　Schenck, J.F. Safety of strong, static magnetic fields. *J. Magn. Reson. Imaging* **2000**, *12*, 2–19. [CrossRef]

21.　Shellock, F.G.; Shellock, V.J. Cardiovascular catheters and accessories: Ex vivo testing of ferromagnetism, heating, and artifacts associated with MRI. *J. Magn. Reson. Imaging* **1998**, *8*, 1338–1342. [CrossRef] [PubMed]

22.　Schueler, B.A.; Parrish, T.B.; Lin, J.C.; Hammer, B.E.; Pangrle, B.J.; Ritenour, E.R.; Kucharczyk, J.; Truwit, C.L. MRI compatibility and visibility assessment of implantable medical devices. *J. Magn. Reson. Imaging* **1999**, *9*, 596–603. [CrossRef]

23.　New, P.F.; Rosen, B.R.; Brady, T.J.; Buonanno, F.S.; Kistler, J.P.; Burt, C.T.; Hinshaw, W.S.; Newhouse, J.H.; Pohost, G.M.; Taveras, J.M. Potential hazards and artifacts of ferromagnetic and nonferromagnetic surgical and dental materials and devices in nuclear magnetic resonance imaging. *Radiology* **1983**, *147*, 139–148. [CrossRef] [PubMed]

24.　Shellock, F.G.; Crues, J.V. High-field-strength MR imaging and metallic biomedical implants: An ex vivo evaluation of deflection forces. *AJR Am. J. Roentgenol.* **1988**, *151*, 389–392. [CrossRef] [PubMed]

25. Kagetsu, N.J.; Litt, A.W. Important considerations in measurement of attractive force on metallic implants in MR imagers. *Radiology* **1991**, *179*, 505–508. [CrossRef] [PubMed]
26. Dedini, R.D.; Karacozoff, A.M.; Shellock, F.G.; Xu, D.; McClellan, R.T.; Pekmezci, M. MRI issues for ballistic objects: Information obtained at 1.5-, 3- and 7-Tesla. *Spine J.* **2013**, *13*, 815–822. [CrossRef] [PubMed]
27. Shellock, F.G.; Morisoli, S.M. Ex vivo evaluation of ferromagnetism, heating, and artifacts produced by heart valve prostheses exposed to a 1.5-T MR system. *J. Magn. Reson. Imaging* **1994**, *4*, 756–758. [CrossRef] [PubMed]
28. Shokrollahi, P.; Drake, J.M.; Goldenberg, A.A. Measuring the temperature increase of an ultrasonic motor in a 3-tesla magnetic resonance imaging system. *Actuators* **2017**, *6*, 20. [CrossRef]
29. Shokrollahi, P.; Drake, J.M.; Goldenberg, A.A. Ultrasonic motor-induced geometric distortions in magnetic resonance images. *Med. Biol. Eng. Comput.* **2017**. [CrossRef] [PubMed]
30. Shokrollahi, P.; Drake, J.M.; Goldenberg, A.A. Signal-to-noise ratio evaluation of magnetic resonance images in the presence of an ultrasonic motor. *Biomed. Eng. Online* **2017**, *16*, 45. [CrossRef] [PubMed]